GOALS: THE GREAT OBSERVATORIES ALL-SKY LIRG SURVEY

L. Armus[1], J.M. Mazzarella[2], A.S. Evans[3,4], J.A. Surace[1], D.B. Sanders[5], K. Iwasawa[6], D.T. Frayer[7], J.H. Howell[1], B. Chan[2], A.O. Petric[1], T. Vavilkin[8], D.C. Kim[3], S. Haan[1], H. Inami[9], E.J. Murphy[1], P.N. Appleton[6], J.E. Barnes[4], G. Bothun[10], C.R. Bridge[1], V. Charmandaris[11], J.B. Jensen[12], L.J. Kewley[4], S. Lord[2], B.F. Madore[2,13], J.A. Marshall[14], J.E. Melbourne[15], J. Rich[4], S. Satyapal[16], B. Schulz[6], H.W.W. Spoon[17], E. Sturm[18], V. U[4], S. Veilleux[19], K. Xu[6]

ABSTRACT

The Great Observatories All-sky LIRG Survey (GOALS[*]) combines data from NASA's Spitzer, Chandra, Hubble and GALEX observatories, together with ground-based data into a comprehensive imaging and spectroscopic survey of over 200 low redshift ($z < 0.088$), Luminous Infrared Galaxies (LIRGs). The LIRGs are a complete subset of the IRAS Revised Bright Galaxy Sample (RBGS), which comprises 629 extragalactic objects with 60μm flux densities above 5.24 Jy, and Galactic latitudes above five degrees. The LIRGs targeted in GOALS span the full range of nuclear spectral types defined via traditional optical line-ratio diagrams (type-1 and type-2 AGN, LINERs, and starbursts) as well as interaction stages (major mergers, minor mergers, and isolated galaxies). They provide an unbiased picture of the processes responsible for enhanced infrared emission in galaxies in the local Universe. As an example of the analytic power of the multi-wavelength GOALS dataset, we present Spitzer, Chandra, Hubble and GALEX images and spectra for the interacting system VV 340 (IRAS F14547+2449). The Spitzer MIPS imaging data indicates that between $80 - 95\%$ of the total far-infrared emission (or about $5 \times 10^{11} L_\odot$) originates in VV 340 North. While the Spitzer IRAC colors of VV 340 North and South are consistent with star-forming galaxies, both the Spitzer IRS and Chandra ACIS data indicate the presence of an AGN in VV 340 North. The observed line fluxes, without correction for extinction, imply the AGN accounts for less than $10 - 20\%$ of the observed infrared emission. The X-ray data are consistent with a heavily absorbed ($N_H \geq 10^{24} cm^{-2}$) AGN. The GALEX far and near-UV fluxes imply a extremely large infrared "excess" (IRX) for the system ($F_{IR}/F_{fuv} \sim 81$) which is well above the correlation seen in starburst galaxies. Most of this excess is driven by VV 340 N, which has an IR excess of nearly 400. The VV 340 system seems to be comprised of two very different galaxies – an infrared luminous edge-on galaxy (VV 340 North) that dominates the long-wavelength emission from the system and which hosts a buried AGN, and a face-on starburst (VV 340 South) that dominates the short-wavelength emission.

Subject headings: Galaxies

[1] Spitzer Science Center, Calfornia Institute of Technology, MS 220-6, Pasadena, CA 91125
[2] Infrared Processing and Analysis Center, Calfornia Institute of Technology, MS 100-22, Pasadena, CA 91125
[3] National Radio Astronomy Observatory, 520 Edgemont Road, Charlottesville, VA 22903
[4] Department of Astronomy, University of Virginia, P.O. Box 400325, Charlottesville, VA 22904
[5] Institute for Astronomy, University of Hawaii, 2680 Woodlawn Drive, Honolulu, HI 96822
[6] INAF-Observatorio Astronomico di Bologna, Via Ranzani 1, Bologna, Italy
[7] NASA Herschel Science Center, California Institute of Technology, MS 100-22, Pasadena, CA 91125
[8] Department of Physics and Astronomy, SUNY Stony Brook, Stony Brook, NY, 11794
[9] Department of Space and Astronautical Science, The Graduate University for Advanced Studies, Japan
[10] Physics Department, University of Oregon, Eugene OR, 97402
[11] Department of Physics, University of Crete, P.O. Box 2208, GR-71003, Heraklion, Greece
[12] Gemini Observatory, 940 N. Cherry Ave., Tucson, AZ, 85719
[13] The Observatories, Carnegie Institute of Washington, 813 Santa Barbara Street, Pasadena, CA 91101
[14] The Jet Propulsion Laboratory, California Institute of Technology, Pasadena, CA 91125
[15] California Institute of Technology, MS 320-47, Pasadena, CA 91125
[16] Department of Physics & Astronomy, George Mason University, 4400 University Drive, Fairfax, VA 22030
[17] Department of Astronomy, Cornell University, Ithaca, NY, 14953

1. INTRODUCTION

The Infrared Astronomical Satellite (IRAS) provided the first unbiased survey of the sky at mid and far-infrared wavelengths, giving us a comprehensive census of the infrared emission properties of galaxies in the local Universe. The high luminosity tail of the infrared luminosity function can be approximated by a power-law ($L_{IR}^{-2.35}$), which implies a space density for the most luminous infrared sources which is well in excess of what is found in the optical for local galaxies (e.g., Schechter 1976). At the highest luminosities, Ultraluminous Infrared Galaxies, or ULIRGs (those galaxies with $L_{IR} > 10^{12}$ L$_\odot$) have a space density that is a factor of $1.5 - 2$ higher than that of optically selected QSOs, the only other known objects with comparable bolometric luminosities (Schmidt & Green 1983).

Multi-wavelength imaging surveys have shown that nearly all ULIRGs are found in systems which have undergone strong tidal perturbations due to the merger of pairs of gas-rich disk galaxies (Armus et al. 1987; Sanders et al. 1988a,b; Murphy et al. 1996,2001a).

[18] MPE, Postfach 1312, 85741 Garching, Germany
[19] Astronomy Department, University of Maryland, College Park, MD 20742
[*] http://goals.ipac.caltech.edu

They have enhanced star formation rates compared to non-interacting galaxies, and the fraction of sources with active galactic nuclei (AGN) increases as a function of increasing L_{IR} (Armus, et al. 1989; Murphy et al. 1999,2001b; Veilleux et al. 1995,1997; Kim et al. 1998). ULIRGs may represent an important evolutionary stage in the formation of QSOs (e.g., Sanders et al. 1988a,b) and perhaps powerful radio galaxies (Mazzarella et al. 1993; Evans et al. 2005). In fact, numerical simulations have shown that tidal dissipation in mergers can be very effective in driving material from a gas-rich galaxy disk towards the nucleus, fueling a starburst and/or a nascent AGN (e.g., Barnes & Hernquist 1992). Morphological and kinematic studies of ULIRGs also suggest that their stellar populations are evolving into relaxed, elliptical-like distributions (Wright, et al. 1990; Genzel et al. 2001; Tacconi et al. 2002).

Luminous Infrared Galaxies, or LIRGs (those galaxies with $L_{IR} \geq 10^{11}$ $L_{\odot}$), are interesting phenomena in their own right, but they also may play a central role in our understanding of the general evolution of galaxies and black holes, as demonstrated by two key observational results. First, observations with ISO and Spitzer have shown that LIRGs comprise a significant fraction ($\geq 50\%$)of the cosmic infrared background and dominate the star-formation activity at $z \sim 1$ (Elbaz et al. 2002; Le Floc'h et al. 2005; Caputi et al. 2007, Magnelli et al. 2009). In comparison to the local universe where they are relatively rare, ULIRGs are about a thousand times more common at $z \gtrsim 2$ (Blain et al. 2002; Chapman et al. 2005). Second, the ubiquity of super-massive nuclear black holes in quiescent galaxies and the scaling of their masses with stellar bulge masses (Magorrian et al. 1998; Ferrarese & Merritt 2000; Gebhardt et al. 2000) suggest an intimate connection between the evolution of massive galaxies and their central black holes. One explanation for the relationship is that mass accretion onto the black hole occurs during episodes of nuclear star formation. The study of a large, complete sample of local LIRGs spanning all merger and interaction stages can shed critical light on the co-evolution of black holes and stellar bulges in massive galaxies.

The Great Observatories All-sky LIRG Survey (GOALS) combines data from NASA's Spitzer, Hubble, Chandra and GALEX observatories in a comprehensive imaging and spectroscopic survey of over 200 low redshift ($z < 0.088$) LIRGs (see Table 1). The primary new data sets consist of Spitzer IRAC and MIPS imaging, IRS spectroscopy, HST ACS, NICMOS, and WFPC2 imaging, Chandra ACIS imaging, and GALEX far and near-UV observations. The majority of the new observations are being led by GOALS team members, but we also make use of the Spitzer, HST, Chandra and GALEX archives to fill out the sample data (see Table 2). In addition, optical and K-band imaging (Ishida et al. 2004), optical spectra (Kim et al. 1995), J, H, and Ks-band near-infrared images from 2MASS (Skrutskie et al. 2006), sub-millimeter images (Dunne et al. 2000), CO and HCN (Sanders, Scoville & Soifer 1991; Gao & Solomon 2004), and 20cm VLA imaging (Condon et al. 1990) exist for various sub-sets of the LIRGs in GOALS, besides the IRAS data with which the sources were selected (Sanders et al. 2003). In this paper we introduce the main components of the survey, present our primary

science objectives, and discuss the multi-wavelength results for one source, VV 340. The layout of the paper is as follows. The scientific objectives are discussed in section 2, followed by a definition of the sample in section 3. In section 4 we describe the observations, in section 5 we outline the Spitzer Legacy data products being delivered, and in section 6 we present results for the LIRG VV 340.

2. SCIENTIFIC OBJECTIVES OF GOALS

While a great deal of effort has been devoted to the study of ULIRGs, LIRGs have, in comparison, suffered from a lack of attention. Ground-based optical and near infrared imaging studies of low-redshift LIRGs have been performed (e.g., Ishida 2004), but multi-wavelength imaging and spectroscopic surveys of a large sample of the nearest and brightest LIRGs have not been completed. This is undoubtedly due to the fact that LIRGs form a morphologically diverse group of galaxies, unlike ULIRGs which are nearly always involved in the final stages of a violent and spectacular merger. LIRGs are also much harder to detect and analyze at high redshift in many shallow surveys, which has traditionally removed much of the impetus behind establishing a robust library of low-redshift analogs. This has changed recently, with surveys such as COSMOS (Scoville et al. 2007) and GOODS (Dickinson et al. 2003), which include significant samples of LIRGs at cosmologically interesting epochs.

An important question regarding the nature of LIRGs, is what is the source of their power? What mechanism is responsible for generating energy at a rate that is tens to hundreds of times larger than emitted by a typical galaxy? Interactions between large, late-type galaxies are evident in many systems, but a significant fraction of LIRGs show no morphological evidence (e.g., double nuclei, tidal tails or stellar bridges, etc.) for a major merger. Large molecular gas masses, large gas fractions, or unusual dynamics may all play a role. Regardless of the trigger, an AGN or an intense starburst is often invoked as the most likely source of the energy in LIRGs. The relative importance of AGN and starburst activity within individual systems, for the generation of far-infrared radiation from LIRGs as a class, and how the dominant energy source changes as a function of merger stage are all important questions that can only be answered by studying a large, unbiased sample at a wide variety of wavelengths. This is the primary motivation behind the GOALS project.

By their very nature, LIRGs are dusty galaxies, wherein a large fraction (over 90% for the most luminous systems) of the UV light emitted by stars and/or AGN is absorbed by grains and re-radiated in the far-infrared. This makes traditonal, UV and optical spectroscopic techniques for detecting and measuring starbursts and AGN (e.g., emission line ratios and linewidths) difficult to link quantitatively to the ultimate source of the IR emission. However, by combining these data with observations in the infrared, hard x-ray, and radio, it is possible to penetrate the dust and better understand the LIRG engine.

With the IRAS data we have been able to construct unbiased, flux-limited samples of LIRGs and measure their global far-infrared colors, albeit with little or no informa-

tion about the distribution of the dust, due to the large IRAS beam sizes. The overall LIRG Spectral Energy Distributions (SEDs) are shaped by the relative locations of the dust and the young stars, as well as the presence of an active nucleus. At a basic level, the size of the warm dust emiting region can give an indication of the power source, since a starburst will be spread out on kpc scales while the region heated by an AGN will be $2-3$ orders of magnitude smaller. Spitzer imaging with IRAC and MIPS can give us our first estimates of the size of the IR-emitting regions in the nearest LIRGs, although higher spatial resolution is required for the vast majority of systems if we are to place meaningful constraints on, for example, the luminosity density of the nuclear starburst. Ground-based $10-20\mu$m imaging can provide a high spatial resolution view of the nucleus, but these wavelengths are most sensitive to the hottest dust, and extrapolations to the far-infrared are always required. The IRAC data provides the finest spatial resolution on Spitzer, and since the IRAC bands for low-redshift galaxies are dominated by stars, hot dust, and finally PAH emission as one progresses from 3.6μm to 8μm, the nuclear colors themselves can indicate the presence of an AGN (Lacy et al. 2004; Stern et al. 2005). Although the spatial resolution of the MIPS data is limited, the flux ratios give an indication of the dust temperature and hence, the importance of an AGN to the overall energy budget. When coupled with the radio continuum data, the MIPS fluxes can also be used to estimate the radio–far-infrared flux ratio, itself an indicator of the presence of a (radio loud) AGN.

Mid-infrared and X-ray spectroscopy provide powerful tools for not only uncovering buried AGN, but also measuring the physical properties of the gas and dust surrounding the central source. The low-resolution IRS spectra are ideal for measuring the broad PAH features at 6.2, 7.7, 8.6, 11.3, and 12.7μm, the silicate absorption features at 9.7 and 18μm, and water or hydrocarbon ices at $5-7\mu$m (e.g., Spoon et al. 2004; Armus et al. 2007). The PAH ratios indicate the size and ionization state of the small grains (e.g., Draine & Li 2001), while the silicate absorption gives a direct measure of the optical depth towards the nuclei and clues as to the geometry of the obscuring medium (e.g. Levenson et al. 2007, Sirocky et al. 2008). The ratio of the PAH emission to the underlying (hot dust) continuum can be used as a measure of the strength of an AGN, since Seyfert galaxies and quasars typically have extremely low PAH equivalent widths (EQW) compared to starburst galaxies (Genzel et al. 1998; Sturm et al. 2002, Armus et al. 2004,2006,2007). Among ULIRGs, the PAH EQW have even been shown to decrease with increasing luminosity (Tran et al. 2001; Desai et al. 2007) suggesting an increasing importance of an AGN in the highest luminosity systems. Since the strengths of the PAH features can dominate broad-band, mid-infrared filter photometry, it is critical to understand how the relative strengths of the PAH features vary within the LIRG population and how they affect the colors with redshift (see Armus et al. 2007). In addition, the shape of the silicate absorption can indicate the presence of crystalline silicates, themselves a clear sign of violent, and recent, grain processing (e.g., Spoon et al. 2006).

The high-resolution IRS spectra are ideally suited for measuring the equivalent widths and relative line strengths of the narrow, fine-structure atomic emission lines such as [S IV] 10.5μm, [Ne II] 12.8μm, [Ne III] 15.5μm, [Ne V] 14.3 and 24.3μm , [O IV] 25.9μm, [S III] 18.7 and 33.5μm , [Si II] 34.8μm, [Fe II] 17.9 and 25.9μm, as well as the pure rotational H_2 lines at 9.66μm, 12.1μm, 17.0μm and 28.2μm. These lines provide a sensitive measure of the ionization state and density of the gas, and they can be also used to infer the basic properties (e.g., T_{eff}) of the young stellar population. The H_2 lines probe the warm (100-500 K) molecular gas and, when combined with measurements of the cold molecular gas via the mm CO line, can be used to infer the warm-to-cold molecular gas fraction as a function of evolutionary state (e.g. Higdon et al. 2007). The high resolution spectra can also indicate the presence of a warm, interstellar medium, via absorption features of C_2H_2 and HCN at 13.7μm and 14.0μm, respectively (see Lahuis et al. 2007).

The low background of the ACIS detector, together with the excellent spatial resolution of Chandra, provide an unprecedented view of the $0.4-8$ keV X-ray emission in LIRGs. X-ray binaries, an AGN, and hot gas associated with an outflowing wind can all contribute to the measured X-ray emission on different physical scales and at different characteristic energies. The X-ray images will allow us to quantify the amount and extent of resolved X-ray emission in LIRGs as an indication of extent of the starburst, and/or the presence of an outflowing wind. The winds are driven through the combined action of overlapping supernovae, producing both a hot central component and soft, extended emission, made up predominantly of shocked, swept-up gas in the ISM (e.g., Fabbiano, Heckman & Keel 1990; Heckman et al. 1990; Armus et al. 1995; Read, Ponman & Strickland 1997; Dahlem, Weaver & Heckman 1998; Strickland et al. 2004a,b). An AGN, on the other hand, will produce unresolved hard X-ray emission, sometimes accompanied by a strong neutral or ionized iron line.

The penetrating power of the hard X-rays implies that even obscured AGN should be visible to Chandra (e.g., Komossa et al. 2003). Unresolved, hard X-ray ($2-8$ keV) flux with strong iron line emission is a clear indication of an AGN, and by fitting the spectrum we can derive both the intrinsic luminosity and the HI column toward the accretion disk(s). Of course, identifying the true nature of the nuclear emission from the Chandra spectra alone is difficult for sources where the HI column density exceeds $\sim 10^{24}$cm^{-2}, but the combination of X-ray spectral and spatial information can help disentangle the extended starburst emission from the unresolved, harder emission from an AGN in many LIRGs. Of particular interest among the LIRG sample is whether or not the X-ray luminosity can be used as a quantitative measure of the star formation rate. In galaxies dominated by star formation, where the X-ray emission is dominated by high-mass X-ray binaries, there is a correlation between the X-ray luminosity and the star formation rate as measured by the infrared or radio emission (Ranalli et al. 2003; Grimm et al. 2003). It will be interesting to determine whether or not this relation holds for the powerful starbursts found in LIRGs.

The radio emission from galaxies is immune to the effects of dust obscuration, and the far-infrared to radio flux ratio, q (Helou et al. 1985), shows a tight corre-

lation for star-forming galaxies (Yun, Reddy & Condon 2001). In addition, the radio spectral index and the radio morphology can be used to identify buried AGN and/or jets in the nuclei of LIRGs at the high spatial resolution afforded with the VLA. The available GHz radio data for the GOALS sample (Condon et al. 1990) will therefore provide a critical baseline for understanding the power sources and the ISM properties of the GOALS sample. In particular, it will be valuable to compare the radio and far-infrared morphologies of the nearest LIRGs and explore the far-infrared – radio correlation in detail within luminous infrared galaxies, such has been done for other nearby samples (e.g., Murphy et al. 2006).

In addition to uncovering buried AGN and nuclear starbursts in LIRGs, GOALS provides an excellent opportunity to study star-formation in LIRG disks as a function of merger stage. The wide wavelength coverage and sensitivity provide a detailed look at the old and young stars, the dust, and the gas across the merger sequence. GOALS will allow us to answer some important questions about galactic mergers, such as, what fraction of the star-formation occurs in in extra-nuclear (super) star clusters? Can the ages and locations of these clusters be used to reconstruct the merger history and refine detailed models of the merger process and what are the physical processes that drive star-formation on different scales in the merger? A simple question that still needs to be addressed is the range in UV properties of LIRGs. Are LIRGs as a class, weak or strong UV emitters? How much of the ionizing flux emerges, and is the ratio of IR to UV emission related to any of the other properties, e.g. the merger state or the distribution of the dust?

GALEX has provided our first look at the properties of large numbers of UV-selected starburst and AGN as a function of cosmic epoch (e.g., Gil de Paz, et al. 2007; Xu, et al. 2007; Martin, et al. 2007; Schiminovich, et al. 2007). By combining the GALEX and Spitzer data, we will be able to make a full accounting of the energy balance throughout the GOALS sample, relating the UV emission to the infrared photometric and spectroscopic properties of a complete sample of low-redshift LIRGs. In the GOALS targets that are resolved by GALEX (a small but important sub-sample), we will be able to separate the nucleus and disk in single systems, and the individual galaxies in interacting systems, in order to measure the relative UV emission escaping from the systems and directly compare this to the far-infrared emission measured with Spitzer. This will provide a detailed look at the variation in the IR to UV ratio within interacting galaxies at all stages.

The HST imaging data in GOALS provides our sharpest look at the stellar clusters and detailed morphological features in LIRGS. The depth and high spatial resolution of the HST imaging with the Advanced Camera for Surveys (ACS) Wide Field Camera (WFC) allows for a sensitive search for faint remnants of past, or less-disruptive (minor) mergers (e.g., shells, fading tails, etc.), small scale nuclear bars, and even close, double nuclei, although the latter are notoriously difficult to measure at optical wavelengths in heavily obscured systems. These data will be used to fit models of galaxy surface brightness profiles with standard programs (e.g., GALFIT) and estimate basic structural parameters (e.g. bulge to disk ratio, half-light radius) for the LIRGs as a class, and as

a function of nuclear properties (e.g., AGN or starburst dominated spectra as determined from the Spitzer IRS and Chandra data).

The sub-arcsec resolution of the ACS also allows a sensitive search for and quantitative measurement of the young, star-forming clusters in LIRGs. The cluster populations can be placed on color magnitude diagrams in order to estimate their ages, and the number and luminosity of such systems can be studied as a function of the relative age of the merger. Particularly powerful in studying the cluster ages will be the combination of visual and UV imaging with ACS (the latter obtained with the Solar Blind Channel, SBC) since the colors will then allow us to break the age-reddening degeneracy over a large range in cluster ages ($10^6 - 10^8$ yrs). The cluster results can then be compared to models of the interaction, as has been done in some well-studied mergers (e.g., NGC 4038/9 – Whitmore & Schweizer 1995; Whitmore, et al. 2005,2007; Mengel, et al. 2001,2005). For example, it has recently been shown that while the interacting LIRG NGC 2623 posesses a large number of young star clusters that probably formed in the interaction, they account for a negligible fraction ($< 1\%$) of the bolometric luminosity (Evans et al. 2008).

Our understanding of the UV emission properties of LIRGs will be greatly enhanced by the addition of the high-resolution ACS far-UV imaging data. Only a handful of LIRGs have been imaged in the vacuum ultraviolet at high resolution (e.g. Goldader et al. 2002). Although the study of the cluster populations is the primary scientific goal for the ACS imaging, they will be extremely valuable for understanding the physical conditions that drive luminous infrared galaxies away from the well-known IRX-β correlation - the correlation between infrared excess and UV spectral slope (see Meurer et al. 1999; Goldader et al. 2002). ULIRGs fall well off the correlation established for starburst galaxies, and this is usually interpreted simply as disconnect between the sources of the observed UV and far-infrared emission caused by dust obscuration. However, the physical conditions over which this occurs, and when this sets in during the merger process is not known. By combining the ACS, GALEX and Spitzer imaging data, we will be able to greatly extend the luminosity range over which the UV (and IR) emission has been mapped, as well as sample galaxies along the merger sequence.

To understand the true stellar distribution in the dusty circumnuclear regions in LIRGs, it is important to combine high resolution and long-wavelength imaging. The sub-arcsecond HST NICMOS imaging in GOALS will provide us with our clearest picture of the stellar mass in the LIRG nuclei, and allow us to accurately de-redden the stellar clusters seen in the ACS data. With these data we will be able to search for very small scale, extremely red point sources which may be buried AGN, and find secondary nuclei hidden from even the deepest ACS optical observations. In addition, we will be able to find optically faint or even invisible clusters around the nuclei, and together with the ACS data, assemble a true cluster luminosity function unaffected by dust. The H-band imaging provides us with the best (existing) near-infrared imaging resolution, and it samples the peak in the stellar light curve for the old stars which will dominate the mass in these galaxies. While the NICMOS F160W and the

IRAC 3.6μm data are both effective tracers of the old stars and stellar mass, the NICMOS data have a spatial resolution which is an order of magnitude higher - on the order of 100 pc or better for many of the LIRGs. By combining the IRAC imaging of the entire sample with the NICMOS imaging of the luminous GOALS systems, we will be able to trace the stellar masses from the largest to the smallest scales.

A basic result from the Spitzer imaging in GOALS will be a much better understanding of the distribution of the dust in mergers. Since many of the LIRGs are interacting, yet not fully merged, the IRAC and MIPS images allow us to separate the contribution from each galaxy to the total far-infrared flux as measured by IRAS. They also allow us to separate nuclear from disk emission in many systems, pinpointing the location of the enhanced infrared luminosity as a function of merger state. The MIPS images provide a clean separation between the warm dust (T$\sim$ 50 $-$ 100K) at 24μm and 70μm, and the cold dust, which contributes most at 160μm. One of the most remarkable results from ISO was the discovery that most of the far-infrared emission in the merging galaxy NGC 4038/9 (the Antennae) originates from the disk overlap region which is extremely faint in the UV and optical (Mirabel et al. 1998). The Spitzer GOALS images will allow us to find other systems like the Antennae, and determine the frequency of this completely dust-enshrouded starburst state among the LIRG population as a whole.

Taken together, the imaging and spectroscopic data in GOALS will provide the most comprehensive look at the LIRG population in the local Universe. By studying LIRGs from the X-ray through the radio and far-infrared, we can piece together an understanding of the stars, central black holes, and the interstellar-medium in some of the most actively evolving galaxies today. These observations will be invaluable as a local library with which to interpret the limited photometric and spectroscopic information garnered from deep surveys of LIRGs at high-redshift, providing an in-depth glimpse of the co-evolution of starbursts and black holes at late times, and the role of feedback on the ISM of merging galaxies.

3. SAMPLE DEFINITION AND PROPERTIES

The IRAS Revised Bright Galaxy Sample (RBGS; Sanders et al. 2003) is a complete sample of extragalactic objects with IRAS $S_{60} > 5.24$ Jy, covering the full sky above a Galactic latitude of $|b| > 5$ degrees. The RBGS objects are the brightest 60-micron sources in the extragalactic sky, and as such they are the best sources for studying the far-infrared emission processes in galaxies and for comparing them with observations at other wavelengths. The 629 objects in the RBGS all have $z < 0.088$, and near-infrared properties spanning a wide range from normal, isolated gas-rich spirals at low luminosities (L$_{IR} < 10^{10.5}$ L$_{\odot}$) through an increasing fraction of interacting galaxy pairs and ongoing mergers among the more luminous LIRGs and ULIRGs. The sample includes numerous galaxies with optical nuclear spectra classified as starbursts, Type 1 and 2 Seyfert nuclei, and LINERS. The 21 ULIRGs (3%) and 181 LIRGs (29%) in the RBGS form a large, statiscally complete sample of 202 infrared luminous, local galaxies which are excellent analogs for comparisons with infrared and sub-

mm selected galaxies at high redshift. These infrared-luminous sources define a set of galaxies sufficiently large to sample each stage of interaction and provide a temporal picture of the merger process and it's link to the generation of far-infrared radiation. The full sample of LIRGs, along with their basic properties, is listed in Table 1. Note that 77 of the LIRG systems contain multiple galaxies. From this point on we refer to the 202 LIRGs as "systems", comprising approximately 291 individual galaxies. The median distance to the LIRGs in the GOALS sample is 94.8 Mpc. Throughout this paper we adopt H$_0 = 70$ km s^{-1} Mpc^{-1}, $\Omega_{vacuum} = 0.72$, and $\Omega_{matter} = 0.28$.

Note that an update to the cosmological parameters, primarily H$_0 = 70$ km s^{-1} Mpc^{-1} (Hinshaw et al. 2009) instead of H$_0 = 75$ km s^{-1} Mpc^{-1}, which was used when the IRAS Revised Bright Galaxy Sample was compiled (RBGS; Sanders et al. 2003), results in 17 additional RBGS sources classified as LIRGs, namely: IRAS F01556+2507 (UGC 01451, $\log(L_{IR}/L_{\odot}) = 11.00$); F02072-1025 (NGC 0839, $\log(L_{IR}/L_{\odot})$=11.01); F04296+2923 ($\log(L_{IR}/L_{\odot}) = 11.04$); F04461-0624 (NGC 1667, $\log(L_{IR}/L_{\odot}) = 11.01$); F06142-2121 (IC 2163, $\log(L_{IR}/L_{\odot}) = 11.03$); NGC 2341, $\log(L_{IR}/L_{\odot}) = 11.17$); F10221-2318 (ESO 500-G034, $\log(L_{IR}/L_{\odot}) = 11.01$); F11122-2327 (NGC 3597, $\log(L_{IR}/L_{\odot}) = 11.05$); F12112-4659 (ESO 267-G029, $\log(L_{IR}/L_{\odot}) = 11.11$); F12351-4015 (NGC 4575, $\log(L_{IR}/L_{\odot}) = 11.02$); F14004+3244 (NGC 5433, $\log(L_{IR}/L_{\odot}) = 11.02$); F14430-3728 (ESO 386-G019, $\log(L_{IR}/L_{\odot}) = 11.01$); F15467-2914 (NGC 6000, $\log(L_{IR}/L_{\odot}) = 11.07$); F17468+1320 (CGCG 083-025; $\log(L_{IR}/L_{\odot}) = 11.05$); F19000+4040 (NGC 6745, $\log(L_{IR}/L_{\odot}) = 11.04$); F22025+4204 (UGC 11898, $\log(L_{IR}/L_{\odot}) = 11.02$); F22171+2908 (Arp 278, $\log(L_{IR}/L_{\odot}) = 11.02$). Since these galaxies were not part of the original LIRG sample drawn from the RBGS, they are not included in GOALS.

4. GOALS OBSERVATIONS

4.1. *Spitzer*

4.1.1. *IRAC and MIPS Imaging*

Of the 202 LIRGs in our complete sample, we have obtained images of 175 with IRAC and MIPS on the Spitzer Space Telescope (PID 3672, PI J. Mazzarella). The remaining 27 LIRGs have been observed through other Spitzer GTO and GO programs and are available in the archive. The LIRGs were imaged with IRAC at 3.6, 4.5, 5.8, and 8.0μm, in high dynamic range (HDR) mode to avoid saturating the bright nuclei. This provided short (1 $-$ 2sec) integrations, in addition to the longer, primary exposures. Typically, five exposures of 30sec each were used, taken in a Gaussian dither pattern. The LIRGs were imaged with MIPS at 24, 70, and 160μm using the Photometry and Super Resolution AORs. Multiple, 3 $-$ 4sec exposures were taken of each source, with two or three mapping cycles being employed at each wavelength. Total integration times at each of the three MIPS wavelengths were 48, 38, and 25sec, respectively. The IRAC and MIPS photometry and images are presented in Mazzarella et al. (2009).

4.1.2. *IRS Nuclear Spectroscopy*

As part of GOALS, we have obtained Spitzer IRS (Houck et al. 2004) spectra for 158 LIRGs in Table 1 (PID 30323, PI L. Armus). Of these, 115 were observed in all four IRS modules (Short-Low, Long-Low, Short-High, and Long-High), while 43 have been observed in three or fewer IRS modules in order to complete the existing archival data and ensure complete coverage for all GOALS targets.

In all cases we have used IRS Staring Mode AORs, employing "cluster target" observations for those sources with well separated ($\Delta r > 10$ arcsec), nearby interacting companions. Among the 158 LIRGs observed, there were a total of 202 nuclei targeted. We have targeted secondary nuclei only when the flux ratio of primary to secondary nucleus (as measured in the MIPS $24\mu m$ data) is less than or equal to five, in order to capture the spectra of the nuclei actively participating in the far-infrared emission of the system. Since we wish to build up a uniform and complete set of nuclear spectra with the IRS, we have elected to observe all sources in staring mode, even though many LIRGs are resolved to Spitzer (predominantly at IRAC wavelengths).

Ramp durations for all modules were selected based upon the measured IRAC and MIPS nuclear flux densities in order to deliver high signal-to-noise spectra for all LIRGs. In all cases we have used at least two cycles per nod position along the slit, and centered the sources using high accuracy blue IRS peak-up on a nearby 2MASS star. In order to mitigate against time-varying warm pixels and measure accurate line equivalent widths in the small high-res slits, we have obtained background sky observations with matched integration times in the SH and LH slits. For most sources, backgrounds for the SL and LL slits are obtained from the non-primary order (sub-slit) when the primary order is on the target. However, for the (11) targets with IRAC $8\mu m$ diameters of 2.0 arcmin or larger, we have obtained off-source backgrounds, as is done for the high-res modules. After background subtraction, residual bad pixels will be removed with the IRSCLEAN software available from the SSC, and spectra will be extracted (from 2D to 1D) using the SPICE software. The first results from the IRS spectral survey are presented in Petric et al. (2009).

4.1.3. IRS Spectral Mapping

In order to produce spectra of the total mid-infrared emission of the systems, and to measure variations within the LIRG disks, we are obtaining IRS low-resolution (SL + LL) spectral maps of 25 LIRGs as part of a Spitzer cycle-5 GO program (PID 50702, PI L. Armus). The target LIRGs were chosen to span a large range in morphological properties (isolated through late stage interactions) while being well-resolved in our IRAC $8\mu m$ images (to ensure adequate area for constructing spatially-resolved spectral maps). Distances to the mapped LIRGs range from 45.5 to 105.8 Mpc, implying projected spatial resolutions at $6\mu m$ of 0.7 to 1.8 kpc. (3.6 arcsec, or two SL pixels). Ten of these systems have two well separated galaxies requiring individual maps, and therefore there are 35 individual maps in the program. In addition, there are 17 LIRGs with IRS spectral mapping data in the Spitzer archive.

All LIRGs will be observed with the SL and LL slits. There are typically $25 - 45$ steps in each SL map, and

$7 - 13$ steps in each LL map, to cover areas in both slits that are $0.5 - 2$ sq. arcminutes on each source. In all cases, step sizes perpendicular to the slits are $1/2$ the width of the slit. The maps are designed to cover the main bodies of the galaxies, but not the tidal tails (for those LIRGs with tails). The SL exposures are all 60 sec per position, while the LL exposures are 30 sec per position. IRS peakups are not used for the mapping observations. The AORs, which include the SL and LL maps, range in time from $0.8 - 6.0$ hrs each, including overheads. The spectral cubes will be assembled, and 1D spectra extracted using the CUBISM software package available from the SSC web site (Smith et al. 2007).

4.2. Hubble

4.2.1. ACS WFC Imaging

The *HST* observations are presently composed of three campaigns. The first component consists of Advanced Camera for Surveys (ACS) observations of all 88 LIRGs with $L_{IR} > 10^{11.4}$ $L_{\odot}$. Many of these LIRGs have tidal structure or widely separately nuclei on scales of tens to a hundred arc-seconds. Thus the Wide Field Channel (WFC), with its $202'' \times 202''$ field of view, was selected to capture the full extent of each interaction in one *HST* pointing. Each LIRG was imaged with both the F435W and F814W filters, with integration times of 20 and 10 minutes, respectively. A total of 88 orbits of ACS/WFC data were obtained (PID 10592, PI A. Evans). The ACS imaging atlas and initial photometric measurements are presented in Evans et al. (2009).

4.2.2. NICMOS Imaging

The second *HST* campaign was designed to provide high-resolution near-infrared observations to recover nuclear structure obscured from view at optical wavelengths. Observations with the Near-Infrared Camera and Multi-Object Spectrometer (NICMOS) of 59 LIRGs in the ACS-observed sample are underway. The data are being collected using camera two (NIC2) with a field of view of $19.3'' \times 19.5''$, using the F160W filter. For most of the observations, one LIRG is observed per orbit, however, there are many cases in which the galaxy pairs are too widely separated to be observed by *HST* in a single orbit. These new data are complemented by pre-existing archival NICMOS data of an additional 29 GOALS LIRGs, thus providing a complete set of NIC2/F160W observations of the 88 LIRGS in the ACS-observed sample. A total of 76 orbits of NICMOS data are being obtained (PID 11235, PI J. Surace).

4.2.3. ACS SBC Imaging

The third *HST* campaign is designed to obtain near- and far-UV data of a subset of 22 of the LIRGs previously observed with the ACS/WFC that possess the highest number of luminous star clusters within their inner $30''$ (i.e., the field-of-view of the Solar Blind Channel, SBC, of ACS). Five of the 22 LIRG systems are in widely separated pairs that require two pointings, so there are 27 galaxies being observed in total. There are three additional LIRGs with adequate far-UV imaging in the HST archives, bringing the total number of LIRG systems in GOALS with far-UV HST data to 25. The UV observations are being obtained by using the ACS/SBC and

WCPC2 Planetary Camera (PC) in combination with the F140LP (far-UV) and F218W (near-UV) filters, respectively. The program (PID 11196, PI A. Evans) consists of three orbits per galaxy, with one orbit devoted to ACS/SBC (four individual integrations in a box pattern), and two orbits devoted to WFPC2 (four indivdual integrations total over both orbits taken in a box pattern). A total of 81 orbits of UV imaging data are being obtained.

4.3. *Chandra*

Currently, the Chandra X-ray Observatory observations of the GOALS targets focuses on those LIRGs with infrared luminosity larger than $10^{11.73} L_\odot$. We observed 26 targets during the Chandra Cycle-8 (PID 8700551, PI D. Sanders). The X-ray imaging observations were carried out using the ACIS-S detector in VFAINT mode with a 15 ks exposure for each target. Combined with the previously observed 18 objects from the archive, the current sample consists of 44 objects. The exposure time for the objects from the archive ranges from 10 ks to 160 ks. ESO203-IG001 is the only galaxy which was not detected. The products available for each source are the contours of a Chandra full-band image overlaid onto the HST/ACS I-band image; X-ray images in the full (0.4-7 keV), soft (0.5-2 keV), and hard (2-7 keV) band images; azimuthally-averaged radial surface brightness profiles in the soft and hard bands; an energy spectrum when sufficient counts are available (typically more than 100 counts). Other basic information is presented in Iwasawa et al. (2009a,b), and Teng et al. (2009), including detected source counts, soft and hard band fluxes and luminosities, the X-ray hardness ratio (as a guide of a rough estimator of the spectral shape), and a measure of spatial extension of the soft X-ray emission.

4.4. *GALEX*

While the LIRGs are, by definition, infrared luminous, they often do have measurable UV fluxes. In fact, due to variations in the spatial distribution of the obscuring dust, a number of well-known (U)LIRGs in GOALS (e.g. Mrk 171, Mrk 266, Mrk 231, Mrk 273, Mrk 617, and Mrk 848) were first identified as starburst galaxies and AGN by the Markarian survey of UV-excess galaxies – a spectroscopic objective-prism survey conducted years before the IRAS survey (e.g., see Mazzarella & Balzano 1986). Of the 202 LIRGs in GOALS, 145 have been observed with the GALEX telescope in the near-UV (2271 Å) and far-UV (1528 Å) filters. Of these, 124 have high signal-to-noise detections in both filters. Most of these images were taken as part of the All sky Imaging Survey (AIS) or the Nearby Galaxy Survey (NGS - see Gil de Paz et al. 2007), with 51 being observed as part of GOALS (GI1-013, PI J. Mazzarella and GI5-038, PI J. Howell). The AIS integration times are short (100 sec), while the NGS and GOALS observations are long, typically a few ksec in duration. Details of the GALEX observations and the UV photometry are presented in Howell et al. (2009).

5. GOALS DATA PRODUCTS

On regular, approximately six month, intervals, Spitzer images and spectra will be delivered to the Spitzer Science Center and made public through their Legacy program web pages. The first delivery is now available through the Spitzer Legacy web pages at the Spitzer Science Center (http://ssc.spitzer.caltech.edu/legacy/all.html), and the Infrared Science Archive (IRSA) at the Infrared Processing and Analysis Center (http://irsa.ipac.caltech.edu). For GOALS, the delivered products include, (1) IRAC image mosaics in all four IRAC bands. Images are single-extension FITS files with a pixel scale of 0.6 arcsec/pixel. (2) MIPS image mosaics in all three MIPS bands. Images are single-extension FITS files, with wavelength-dependent pixels cales – 1.8 arcsec/pixel at $24\mu m$, 4.0 arcsec/pixel at $70\mu m$, and 8.0 arcsec/pixel at $160\mu m$. (3) IRS nuclear spectra in all four low and high-resolution modules. Spectra are delivered in ASCII (IPAC table) format, similar to those produced by the IRS pipelines. (4) Spatial profiles at two positions along the IRS Short-Low slit (the two nod positions), in the $8.6\mu m$ PAH, $10\mu m$ continuum, and $12.8\mu m$ [Ne II] fine-structure emission line. Profiles are provided in ASCII format, in units of e^-/sec for each pixel. Also included in each file are the profiles at the same wavelengths for an unresolved star. The IRAC images are corrected for "banding", "muxbleed", and "column pulldown" effects, as described in the IRAC Data Handbook. The MIPS images are corrected for latents, weak jailbars, and saturation effects, where possible. The IRAC and MIPS mosaics were constructed using MOPEX to align, resample and combine the data. The IRS spectra are extracted from the two-dimensional BCD pipeline products using the SPICE package. A standard "point source" extraction has been used for all sources. The two nod positions and multiple exposures ("cycles") are used to remove residual cosmic rays and/or bad pixels in the spectra.

6. THE LUMINOUS INFRARED GALAXY VV 340

As an example of the utility of the multi-wavelength GOALS data, we present images and spectra of the LIRG, VV 340 (IRAS F14547+2449; Arp 302). VV 340 consists of two large, spiral galaxies, one face-on and one edge-on, separated by approximately 40 arcsec (27.3 kpc). The two spirals are apparently in the early stages of a merger (Bushouse & Stanford 1992, Lo, Gao & Gruendl 1997). This system has an infrared luminosity of $5 \times 10^{11} L_\odot$ (Sanders et al. 2003).

6.1. *Observations and Data Reduction*

IRAC observations of VV 340 were performed on 17 July 2005 (PID 3672). The data were obtained in high dynamic range mode, with a 30 sec frame time and a five position Gaussian dither pattern. MIPS observations of VV 340 were performed on 25 January 2005 (PID 3672). The data were obtained in photometry mode, using the small field size and an integration time of 3 sec in all three (24, 70, $160\mu m$) filters. One cycle was used for 24 and $70\mu m$, with four cycles being used at $160\mu m$.

IRS observations of the two VV 340 nuclei were performed on 17 March 2007 (PID 30323). The data were obtained in staring mode, using the cluster option. A moderate accuracy blue peakup was done on a nearby 2MASS star in order to center the IRS slits on the northern and southern nuclei. On the sky, the IRS Long-low, Short-low, Short-high, and Long-high slits had projected

position angles of 94.1, 177.8, 134.4, and 49.5^o, respectively. The Long-low, Short-low, Short-high and Long-high observations had ramp times of 60, 30, 120 and 240 seconds, respectively. The high-res observations also had corresponding offset sky observations with the same ramp times. The data were reduced using the S15 version of the IRS pipeline at the SSC, and the spectra were extracted using the SPICE software package using the standard, point source extraction aperture.

GALEX near-UV and far-UV observations were performed on 19 May 2005 and 29 April 2007 (PID 13), for a total of 6028 sec and 3042 sec, respectively. VV 340 was observed with the Chandra X-ray Observatory on 17 December 2006 (PID 8700551). An exposure of 14.9 ks was used, yielding 285 net counts.

HST ACS observations of VV 340 were performed on 7 January 2006 (PID 10592). The data were obtained using the WFC in ACCUM mode, in the F435W and F814W filters. Three, 420 sec exposures were taken in the F435W filter and two, 360 sec exposures were taken in the F814W filter using the LINE dither routine. The WFC field of view is 202×202 arcsec, and the pixel size is 0.05 arcsec. The data were run through the standard pipeline processing, which removes instrumental signatures subtracts a dark frame, flat fields the images, removes geometric distortion and applies a flux calibration. Additional cosmic rays were identified and removed using the lacos_im and jcrrej2.cl routines in IRAF (Rhoads 2000; Van Dokkum 2001).

6.2. *Results & Discussion*

The Chandra, GALEX, HST, and Spitzer images of VV 340 are shown in Fig. 1. A false-color image made from the ACS F435W and F814W data is shown in Fig. 2. The thick, flaring dust lane makes VV 340 N much fainter in the UV than VV 340 S, but the disk and bulge are prominent in the IRAC images. Using the ACS images, we have detected 173 unresolved "clusters" in the VV 340 system, with most of these (159, or 92%) being in the spiral arms of VV 340 South. The apparent magnitudes range from $21 - 27$ mag in B, with absolute magnitudes ranging from 9 to -13 mag, and $B - I$ colors of $0.5 - 2$ mag. These colors are typical for the GOALS LIRGs as a class (Vavilkin et al. 2009). Assuming a typical cluster mass of $10^6 M_\odot$, the ages of these clusters are $\leq 10^8$ yrs, uncorrected for reddening. As a whole, the observed clusters in VV 340 South account for 3% of the total B-band light.

The total far-infrared flux densities for the VV 340 system, as measured with MIPS, are 0.43, 9.38, and 15.73 Jy at 24, 70, and 160μm, respectively. The northern galaxy dominates at 24, 70 and 160μm, accounting for approximately 80, 82, and $\sim 95\%$, respectively, of the total emission from the system (the 160μm ratio is uncertain because of the large size of the PSF). For reference, the IRAS 25, 60, and 100μm flux densities for the entire VV 340 system are 0.41, 6.95, and 15.16 Jy (Sanders et al. 2003). It is interesting to note that the ratio of far-infrared fluxes implies that VV 340 South, by itself, is not a LIRG (log $L_{IR} \sim 10.71 L_\odot$).

The IRAC $3.6 - 4.5$ and $5.8 - 8$ colors, as measured in 10 kpc radius apertures centered on the two nuclei are 0.19 and 1.97 mags for VV 340 North, and 0.04 and 1.96 mags for VV 340 South, respectively. The nuclear

(2 kpc radius aperture) colors are slightly redder, being 0.29 and 2.06 mags for VV 340 North, and 0.06 and 2.16 mags for VV 340 South, respectively. Both the large and small aperture measurements place both galaxies in VV 340 outside of the AGN "wedge" in the IRAC color-color diagram of Stern et al. (2005).

The Spitzer IRS low resolution spectra of the northern and southern nuclei are shown in Fig. 3. VV 340 N has a steeper spectrum and a deeper silicate absorption ($\tau_{9.7} \sim 1.3$ for VV 340 N). The PAH emission features are prominent in both galaxies, although the 17μm feature appears much stronger, with respect to the continuum and the fine structure lines, in VV 340 S. Both [Ne V] 14.3 and 24.3μm lines are seen in the high resolution spectrum of VV 340 N, as is the [O IV] 25.9μm line. The line fluxes are 1.2×10^{-17} W m^{-2}, 2.3×10^{-17} W m^{-2}, and 12.3×10^{-17} W m^{-2}, repetively for the [Ne V] 14.3, 24.3μm, and [O IV] 25.9μm lines in VV 340 N. A portion of the Short-high spectra of VV 340 N and S surrounding the location of the [Ne V] 14.3μm emission line is shown in Fig. 4. The [Ne II] 12.8μm line has a flux of 23.4×10^{-17} W m^{-2} in VV 340 N, and 6.1×10^{-17} W m^{-2} in VV 340 S. In VV 340 N, where the 6.2μm PAH EQW is 0.48μm, the [Ne V]/[Ne II] and [O IV]/[Ne II] line flux ratios are consistent with the presence of a weak AGN, contributing less than $10 - 15\%$ of the IR emission, based on scaling from IRS spectra of local AGN and starburst nuclei (see Armus et al. 2007 and references therein). Since the diagnostic ratios are calculated from the nuclear spectrum, this is an upper limit to the contribution from an AGN to the global IR emission in this source. Alternatively, the coronal-line region could be sitting behind at least 50 mag of visual extinction, assuming an intrinsic [Ne V]/[Ne II] flux ratio of unity. This is much larger than that implied by the optical depth at 9.7μm (A$_V \sim 22$ mags) for VV 340 N. There is no [Ne V] detected from VV 340 S ([Ne V]/[Ne II] < 0.04), and the 6.2μm PAH EQW is 0.53μm, comparable to pure starburst galaxies (Brandl et al. 2006). The lack of [Ne V] emission and the strong PAH EQW both suggest that the southern nucleus has no detectable AGN in the mid-infrared.

The H$_2$ S(2), S(1), and S(0) rotational lines at 12.28, 17.03, and 28.22μm are detected in VV 340 N with line fluxes of 5.67×10^{-17} W m^{-2}, 4.56×10^{-17} W m^{-2}, and 1.3×10^{-18} W m^{-2}, respectively. In VV 340 S, only the S(2) and S(1) lines are seen, with fluxes of 4.4×10^{-18} W m^{-2}, and 1.0×10^{-17} W m^{-2}, respectively. Fits to the emission lines imply masses and temperatures for the warm gas components of 1.73×10^7 M$_\odot$ at 530K in VV 340 N, and 7.8×10^6 M$_\odot$ at 310K in VV 340 S. The nuclear warm gas fractions (warm/cold) are then $\sim 3 \times 10^{-4}$ and $\sim 7 \times 10^{-4}$ in VV 340 N and VV 340 S, respectively, using the masses of cold H$_2$ derived by Lo, Gao & Gruendl (1997). However, the large extent of the CO emission, 23 kpc in VV 340 N and 10 kpc in VV 340 S (much larger than the IRS slit widths) suggests that these ratios are probably lower limits for the nuclei. The large extent of the CO, the relatively low infrared luminosity to H$_2$ mass ratio in both galaxies, and the regular kinematics led Lo, Gao & Gruendl to suggest that the VV 340 system is in an early interaction, pre-starburst, phase.

VV 340 has a total (North plus South) UV flux of

17.55 mag and 16.64 mag in the far and near-UV GALEX filters, respectively. The pair has an apparent infrared to UV flux ratio (the infrared excess, or IRX), of 81.3. The measured UV slope, β, is -0.38 on the GALEX system (see Kong et al. 2004), placing VV 340 well above the fit to local starburst galaxies (Meurer et al. 1999; Goldader et al. 2002) by nearly an order of magnitude. As is obvious from Fig.1, most of the UV emission comes from VV 340 South, while most of the IR emission comes from VV 340 North. If we were to place the galaxies on an IRX-β plot individually, the Northern galaxy would have an IRX $\sim$ 398 and a $\beta \sim -0.39$, while the Southern galaxy would have an IRX $\sim$ 17 and a $\beta \sim -0.44$. This would place the Southern source close to the starburst correlation, but the Northern source much farther off the correlation than the system as a whole. A full discussion of where the LIRGs fall on the the IRX-β plot is given in Howell et al. (2009).

VV 340 is detected at both 1.49 and 4.85 GHz with the VLA (Condon et al. 1990; 1995). While both VV 340 N and S are resolved in the VLA C-array data, the A-array data also reveals a nuclear component and two "hotspots" at radii of about five arcsec, oriented N-S, along the edge-on disk of VV 340 N. VV 340 N and VV 340 S have 1.49 GHz flux densities of 86, and 12 mJy, respectively, and 4.85 GHz flux densities of 30 and 3.5 mJy, respectively. The system has a logarithmic far-infrared to radio flux ratio, q (Helou et al. 1985) of $q = 2.02$ dex. This is within 1.5σ of the standard value for star-forming galaxies ($q = 2.34 \pm 0.26$ dex; Yun, Reddy & Condon 2001). VV 340 N and VV 340 S have q values of 2.02 and 2.00 dex, respectively. VV 340 S has a slightly steeper radio spectral index ($\alpha = -1.0$) than does VV 340 N ($\alpha = -0.8$), the latter being comparable to the standard value seen in star-forming galaxies (Condon 1992).

Chandra X-ray imaging of VV 340 is shown in Figs. 5 & 6. While both galaxies are detected, the emission from the southern galaxy is much weaker, and more diffuse. The northern galaxy is clearly resolved in the soft bands ($0.5 - 2$ keV), with a size of nearly 25 arcsec (17 kpc), but shows a hard ($2 - 7$ keV) X-ray point source coincident with the nucleus. The hard X-ray image also shows two faint blobs to the north and south, aligned with the radio structure (Condon et al. 1990).

The X-ray spectrum of VV 340 N (Fig. 7) is dominated by emission-line rich, extended soft X-ray emission but an excess at high energies above 4 keV is evident. In Fig. 7 we compare the Chandra spectrum of VV 340 N to that of the starburst-dominated LIRG VII Zw 31 (Iwasawa et al. 2009b). VII Zw 31 shows no hard-band excess above 4 keV. The hard-band excess in VV 340 N peaks at approximately 6.4 keV in the rest frame, suggesting a pronounced Fe K line. With the limited detected counts, the exact spectral shape cannot be constrained. However, the most likely interpretation for this hard excess is the emission from a heavily absorbed active nucleus with an absorbing column density ($N_{\rm H}$) of 10^{24} cm^{-2} or larger. Note, this is significantly larger than that implied by the silicate optical depth at 9.7μm. If the observed emission is reflected light from a Compton thick AGN, the intrinsic luminosity could be as high as 2×10^{41} erg s^{-1} in the 2-7 keV band. There is also evidence for the 1.8 keV Si line, which could have a contribution from AGN photoionization, although it could also signal the presence of a large number of core-collapse SNe.

Taken together, the Spitzer, Chandra, GALEX, HST, and VLA data suggest that the interacting system VV 340 is composed of two very different galaxies. The edge-on disk of VV 340 North hides a buried AGN seen in the mid-infrared and X-rays, although the apparent contribution of this AGN to the total energy of the galaxy is low. In contrast, VV 340 South is a face-on starburst galaxy that generates an order of magnitude less far-infrared flux, but dominates the short-wavelength UV emission from the system. VV 340 is a LIRG because of the enhanced emission coming from VV 340 N alone. VV 340 seems to be an excellent example of a pair of interacting galaxies evolving along different paths, or at different rates, implying that the details of the interaction can produce LIRGs whose global properties mask the true nature of the emission. This is particularly relevant for merging galaxies viewed at high redshift.

REFERENCES

Armus, L., Heckman, T.M., & Miley, G.K. 1987, AJ, 94, 831.
Armus, L., Heckman, T.M., & Miley, G.K. 1989, ApJ, 347, 727.
Armus, L., et al. 2004, ApJ Suppl., 154, 178.
Armus, L., et al. 2006, ApJ, 640, 204.
Armus, L., et al. 2007, ApJ, 656, 148.
Barnes, J.E., & Hernquist, L. 1992, ARA&A, 30, 705.
Blain, A.W., Smail, I., Ivison, R.J., Kneib, J.-P., & Frayer, D.T. 2002, PhR, 369, 111.
Brandl, B.R., et al. 2006, ApJ, 653, 1129.
Bushouse, H.A., & Stanford, S.A. 1992, ApJS, 79, 213.
Chapman, S.C., Blain, A.W., Smail, I., & Ivison, R.J. 2005, ApJ, 622, 772.
Caputi, K.I., et al. 2007, ApJ, 660, 97.
Condon, J.J., Helou, G., Sanders, D.B. & Soifer 1990, ApJS, 73, 359.
Condon, J.J. 1992, Annual Reviews of Astronomy & Astrophysics, 30, 575.
Condon, J.J., Anderson, E., & Broderick, J.J. 1995, AJ, 109, 2318.
Dahlem, M., Weaver, K.A., & Heckman, T.M. 1998, ApJS, 118, 401.
Desai, V., et al. 2007, ApJ, 669, 810.
Draine, B.T. & Li, A. 2001, ApJ, 551, 807.
Dickinson, M., et al. 2003, in "The Mass of Galaxies at Low and High Redshift" ESO Astrophysics Symposia, edited by R. Bender and A. Renzini, Springer-Verlag, p. 324.
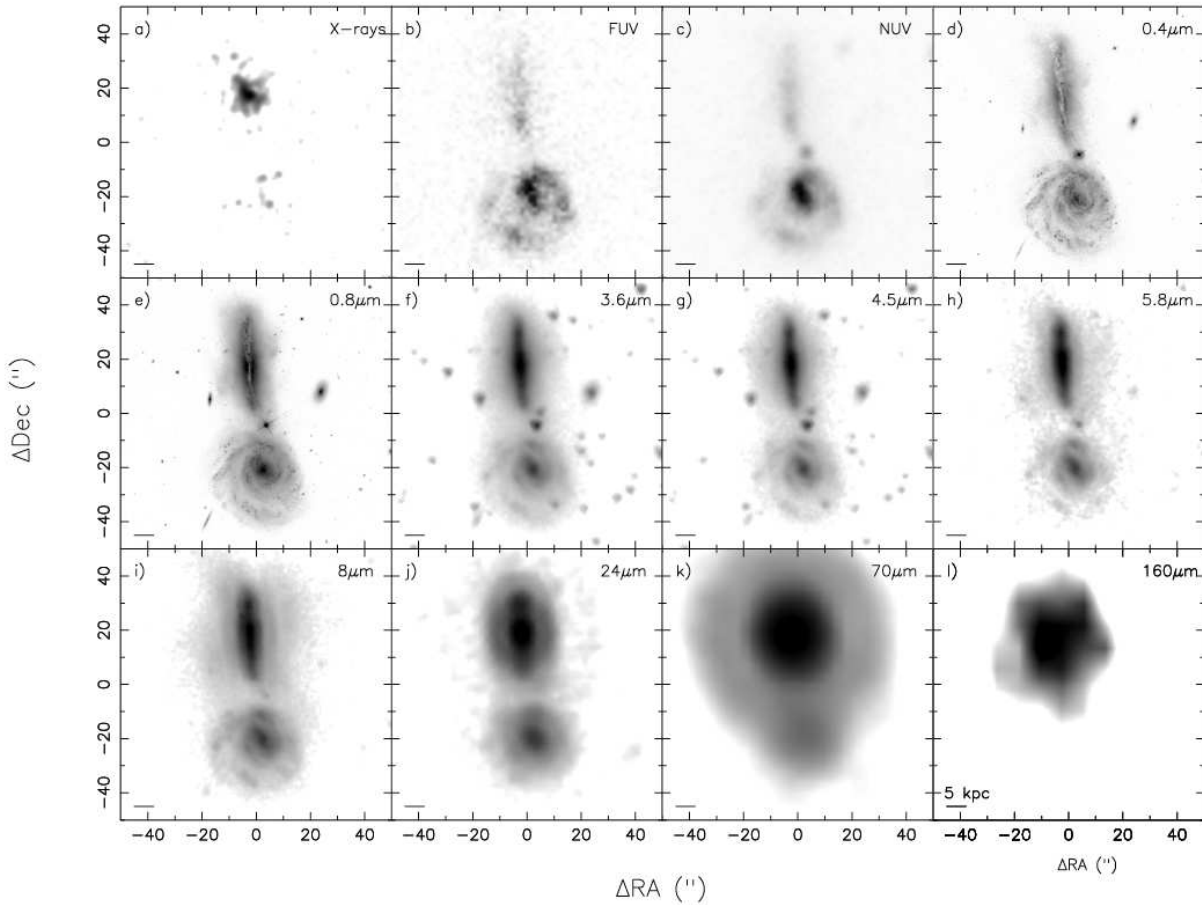
Fig. 1.— Multi-wavelength images of VV 340. From upper left to lower right, these are (a) Chandra $0.4 - 8$ keV, (b) GALEX FUV, (c) GALEX NUV, (d) HST ACS F435W, (e) HST ACS F814W), (f) Spitzer IRAC 3.6μm, (g) Spitzer IRAC 4.5μm, (h) Spitzer IRAC 5.8μm, (i) Spitzer IRAC 8μm., (j) Spitzer MIPS 24μm, (k) Spitzer MIPS 70μm, and (l) Spitzer MIPS 160μm. In all cases a projected linear scale of 5 kpc at the distance of VV 340 is indicated by a bar in the lower left.

Dunne, L., et al. 2000, MNRAS, 315, 115.

Elbaz, D., et al. 2002, A&A, 384, 848.

Evans, A.S., Mazzarella, J.M., Surace, J.A., Frayer, D.T., Iwasawa, K., & Sanders, D.B. 2005, ApJS, 158, 197.

Evans, A.S., et al. 2008, ApJ, 675, 69L.

Evans, A.S., et al. 2009, in preparation.

Fabbiano, G., Heckman, T.M., & Keel, W.C. 1990, ApJ, 355, 442.

Ferrarese, L., & Merritt, D. 2000, ApJ, 539, 9L.

Gao, Y., & Solomon, P.M. 2004, ApJ, 606, 271.

Gebhardt, K., et al. 2000, ApJ, 539, 13L.

Genzel, R., Lutz, D., Sturm, E., Egami, E., Kunze, D., et al. 1998, ApJ, 498, 589.

Genzel, R., Tacconi, L.J., Rigopoulou, D., Lutz, D., & Tecza, M. 2001, ApJ, 563, 527.

Gil de Paz, A., et al. 2007, ApJS, 173, 185.

Goldader, J.D., et al. 2002, ApJ, 568, 651.

Grimm, H.-J., Gilfanov, M., & Sunyaev, R. 2003, MNRAS, 339, 793.

Heckman, T.M., Armus, L., & Miley, G.K. 1990, ApJ Suppl., 74, 833.

Helou, G., Soifer, B.T., & Rowan-Robinson, M. 1985, ApJ, 298, 7L.

Hinshaw, G., et al. 2009, ApJS, 180, 225.

Houck, J.R., et al. 2004, ApJS, 154, 18.

Howell, J.H., et al. 2009, ApJ, submitted.

Ishida, C., 2004 PhD Thesis, University of Hawaii.

Iwasawa, K., Sanders, D.B., Evans, A.S., Mazzarella, J.M., Armus, L., & Surace, J. 2009a, ApJ, 695, 103L.

Iwasawa, K., et al. 2009b, in preparation.

Kim, D.-C., Veilleux, S., & Sanders, D.B. 1998, ApJ, 508, 627.

Kim, D.-C., Sanders, D.B., Veilleux, S., Mazzarella, J.M., & Soifer, B.T. 1995, ApJS, 98, 129.

Komossa, S., et al. 2003, ApJ, 582, 15L.

Kong, X., Charlot, S., Brinchmann, J., & Fall, S.M. 2004, MNRAS, 349, 769.

Lacy, M. et al. 2004, ApJS, 154, 166.

Lahuis, F., et al. 2007, ApJ, 659, 296.

Le Floch, E., et al. 2005, ApJ, 632, 169L.

Levenson, N.A., et al. 2007, ApJ, 654, L45.

Lo, K.Y., Gao, Y., & Gruendl, R.A. 1997, ApJ, 475, L103.

Magnelli, B., et al. 2009, Astronomy & Astrophysics, 496, 57.

Martin, D.C., et al. 2007, ApJS, 173, 415.

Mazzarella, J.M., et al. 2009, in preparation.

Mazzarella, J.M. & Balzano, V.A. 1986, ApJS, 62, 751.

Mazzarella, J.M., Graham, J.R., Sanders, D.B., & Djorgovski, S. 1993, ApJ, 409, 170.

Mengel, S., Lehnert, M.D., Thatte, N., Tacconi-Garman, L., & Genzel, R. 2001, ApJ, 550, 280.

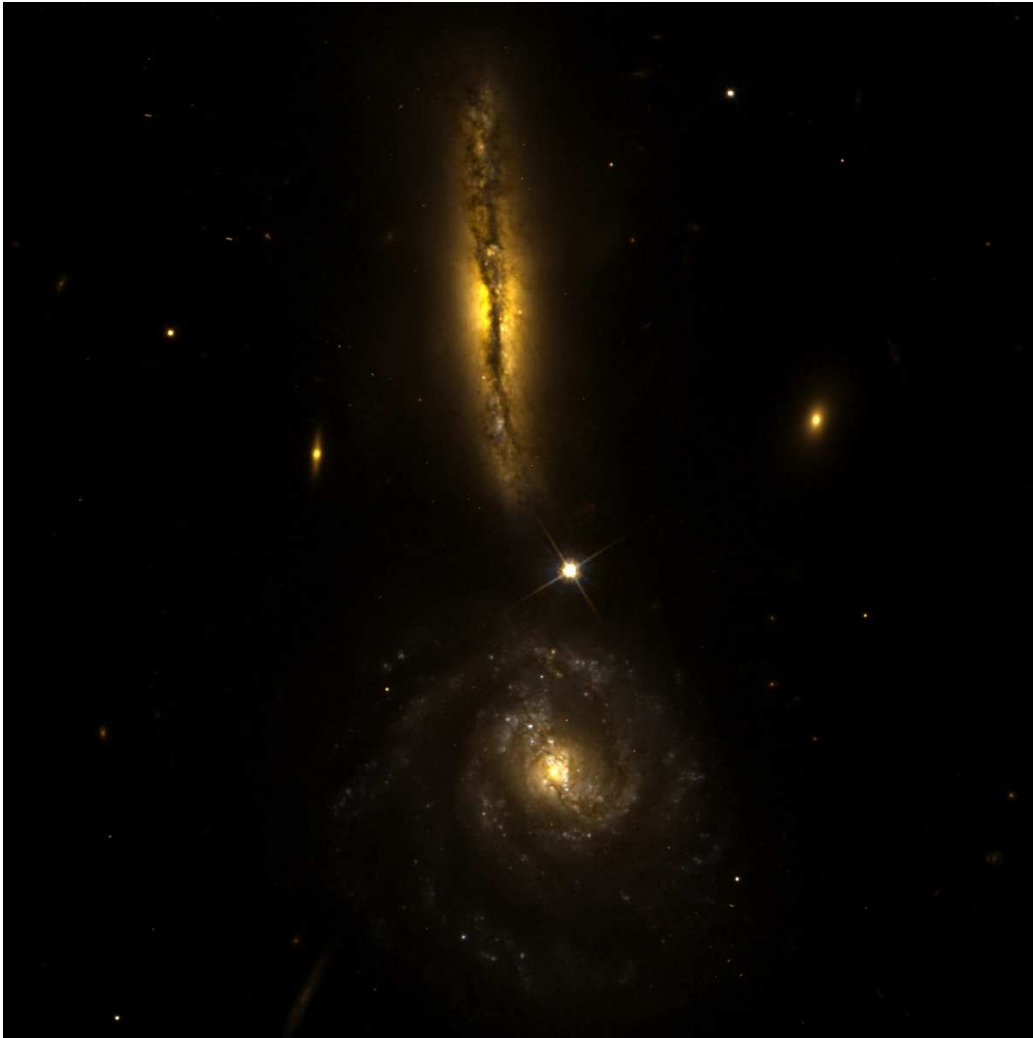Mengel, S., Lehnert, M.D., Thatte, N., & Genzel R. 2005, A & A, 443, 41.

Fig. 2.— False color image of VV 340 (UGC 9618) made from the ACS F435W (blue) and F814W (red) data. The image is approximately 100 arcsec (68 kpc) on a side. North is up and East is to the left.

Meurer, G.R., Heckman, T.M., & Calzetti D. 1999, ApJ, 521, 64.

Mirabel, I.F., et al. 1998, Astronomy & Astrophysics, 333, L1.

Mould, J.R., et al. 2000, ApJ, 529, 786.

Murphy, E.J., et al. 2006, ApJ, 651, L111.

Murphy, T.W. Jr., Armus, L., Matthews, K., Soifer, B.T., Mazzarella, J.M., Shupe, D.L., Strauss, M.A., & Neugebauer, G. 1996, AJ, 111, 1025.

Murphy, T.W. Jr., Soifer, B.T., Matthews, K., Kiger, J.R., & Armus, L. 1999, ApJ, 525, 85L.

Murphy, T.W. Jr., Soifer, B.T., Matthews, K., & Armus, L. 2001a, ApJ, 559, 201.

Murphy, T.W. Jr., Soifer, B.T., Matthews, K., Armus, L., & Kiger, J.R. 2001b, AJ, 121, 97.

Petric, A., et al. 2009, in preparation.

Ranalli, P., Comastri, A., & Setti, G. 2003, A&A, 399, 39.

Read, A.M., Ponman, T.J. & Strickland, D.K. 1997, MNRAS, 286, 626.

Rhoads, J.E. 2000, PASP, 112, 703.

Sanders, D.B., et al. 1988a, ApJ, 325, 74.

Sanders, D.B., Soifer, B.T., Elias, J.H., Neugebauer G., & Matthews, K. 1988b, ApJ, 328, L35.

Sanders, D.B., Scoville, N.Z., & Soifer, B.T. 1991, ApJ, 370, 158.

Sanders, D.B., & Mirabel, I.F. 1996, ARA&A, 34, 749.

Sanders, D.B., Mazzarella, J.M., Kim, D.-C., Surace, J.A., & Soifer, B.T. 2003, AJ, 126, 1607.

Schecter, P. 1976, ApJ, 203, 297.

Schmidt, M., & Green, R.F. 1983, ApJ, 269, 352.

Schiminovich, D., et al. 2007, ApJS, 173, 315.

Scoville, N., et al. 2007, ApJS, 172, 1.

Sirocky, M.M., Levenson, N.A., Elitzur, M., Spoon, H.W.W., & Armus, L. 2008, ApJ, 678, 729.

Skrutskie, M.F., et al. 2006, AJ, 131, 1163.

Smith, J.D., et al. 2007, ApJ, 656, 770.

Spoon, H.W.W., et al. 2004, ApJS, 154, 184.

Spoon, H.W.W., et al. 2006, ApJ, 638, 759.

Stern, D., et al. 2005 ApJ, 631, 163.

Strickland, D.K., Heckman, T.M., Colbert, E.J.M., Hoopes, C.G., and Weaver. K.A. 2004a, ApJS, 151, 193.

Strickland, D.K., Heckman, T.M., Colbert, E.J.M., Hoopes, C.G., and Weaver. K.A. 2004b, ApJ, 606, 829.

Sturm, E., et al. 2002, A & A, 393, 821.

Tacconi, L.J., et al. 2002, ApJ, 580, 73.

Teng, S.H., et al. 2009, ApJ, in press.

Tran, Q.D., et al. 2001, ApJ, 552, 527.

van Dokkum, P.G. 2001, PASP, 113, 1420.

Vavilkin, T., et al. 2009, in preparation.

Veilleux, S., Kim, D.C., Sanders, D.B., Mazzarella, J.M. & Soifer, B.T. 1995, ApJ Suppl., 98, 171.

Veilleux, S., Sanders, D.B., & Kim, D.-C. 1997, ApJ, 484, 92.

Whitmore, B.C., & Schweizer, F. 1995, AJ, 109, 960.

Whitmore, B.C., et al. 2005, AJ, 130, 2104.

Whitmore, B.C., Rupali, C., & Fall, M.S. 2007, AJ, 133, 1067.

Wright, G.S., James, P.A., Joseph, R.D., & McLean, I.S. 1990, Nature, 344, 417.

Xu, C.K., et al. 2007, ApJS, 173, 432.

Yun, M.S., Reddy, N.A., & Condon, J.J. 2001, ApJ, 554, 803.
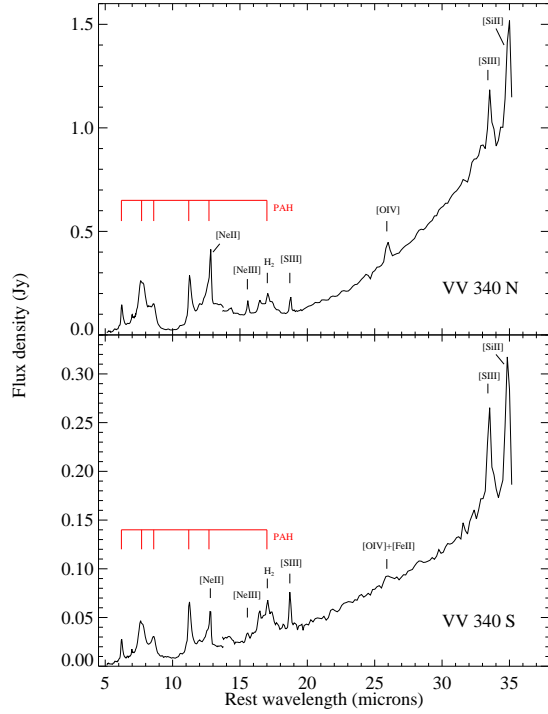
Fig. 3.— IRS low resolution spectra of the nucleus of VV 340 North (above), and South (below). Prominent emission features are marked. The offset at 14μm in the spectrum of VV 340 S is real, and represents a flux difference in the SL and LL spectra for this source, most likely due to significant extended emission in the LL slit.
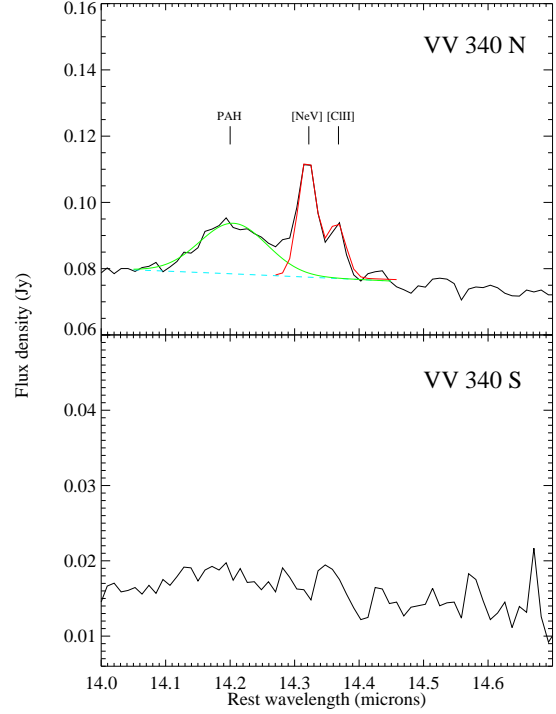
Fig. 4.— IRS Short-high spectra of the nucleus of VV 340 North (above), and South (below) from $14 - 14.7\mu$m in the rest frame. Fits to the PAH 14.22μm emission feature, as well as the [Ne V] 14.322μm, and [Cl II] 14.368μm emission lines indicated in green and red, respectively in VV 340 N, as is the underlying local continuum (blue dashed line). The lines are not detected in VV 340 S.
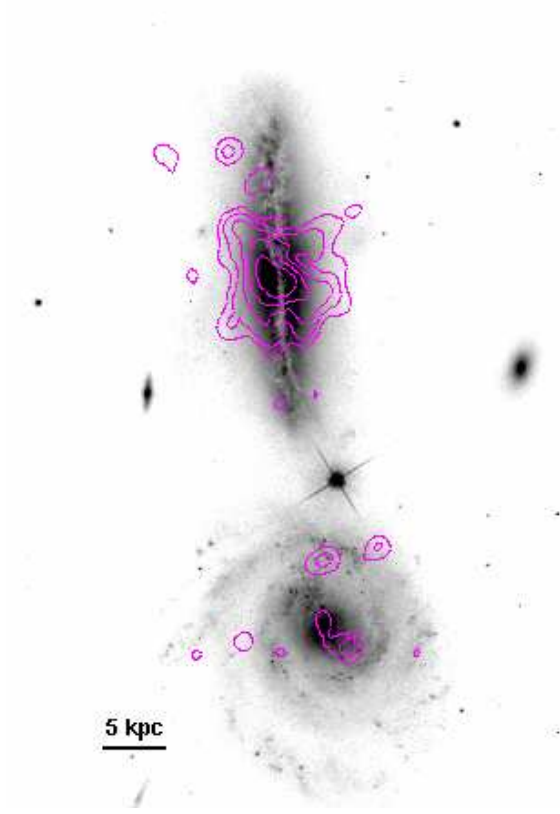
FIG. 5.— Soft $(0.2 - 5$ keV) X-ray image of VV 340 taken with the Chandra X-ray Observatory (contours), overlayed on the HST ACS F435W image (greyscale). North is up, and East is to the left.
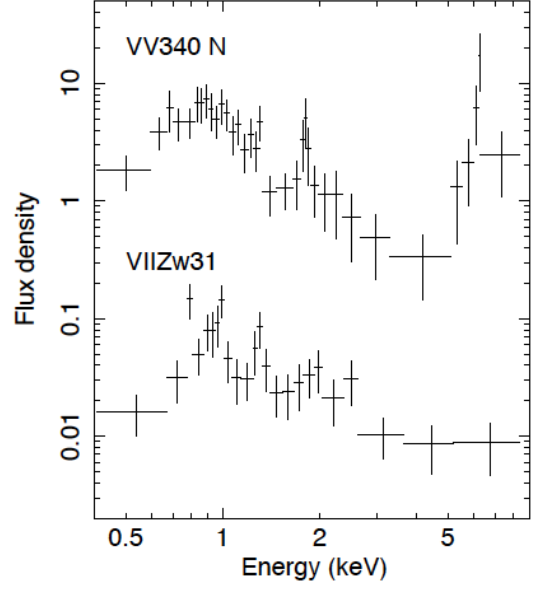
FIG. 7.— The X-ray spectrum of VV 340 North obtained from the ACIS-S. For display purposes, the original data have been re-binned so that each spectral bin contains at least five counts. The vertical axis is in units of 10^{-14}erg cm^{-2} s^{-1} keV^{-1}. Also included for comparison is the ACIS-S spectrum of VII Zw 31 from Iwasawa, et al. (2009b), scaled by 0.02, which is an example of a starburst-dominated LIRG. The hard X-ray excess in VV 340 North is evident at energies above about 4 keV.

FIG. 6.— The soft (left) and hard (right) X-ray images of VV 340 North taken with the Chandra X-ray Observatory. The images have been smoothed with a Gaussian kernel with $\sigma = 2$ pixels. The orientation of the image is North up and East to the left.

TABLE 1
THE GOALS SAMPLE

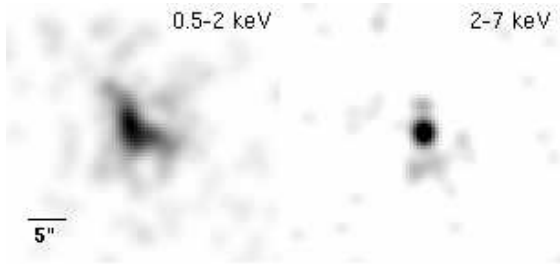| IRAS Name	Optical ID	RA J2000	Dec J2000	V_{Helio} km/s	D_L Mpc	$log(L_{ir}/L_\odot)$
(1)	(2)	(3)	(4)	(5)	(6)	(7)
F00073+2538	NGC 0023	00h09m53.41s	+25d55m25.6s	4566	65.2	11.12
F00085-1223	NGC 0034	00h11m06.55s	-12d06m26.3s	5881	84.1	11.49
F00163-1039	Arp 256	00h18m50.51s	-10d22m09.2s	8159	117.5	11.48
F00344-3349	ESO 350-IG 038	00h36m52.25s	-33d33m18.1s	6175	89.0	11.28
F00402-2349	NGC 0232	00h42m45.82s	-23d33m40.9s	6647	95.2	11.44
F00506+7248	MCG +12-02-001	00h54m03.61s	+73d05m11.8s	4706	69.8	11.50
F00548+4331	NGC 0317B	00h57m40.45s	+43d47m32.1s	5429	77.8	11.19
F01053-1746	IC 1623	01h07m47.18s	-17d30m25.3s	6016	85.5	11.71
F01076-1707	MCG -03-04-014	01h10m08.96s	-16d51m09.8s	10040	144.0	11.65
F01159-4443	ESO 244-G012	01h18m08.15s	-44d27m51.2s	6307	91.5	11.38:
F01173+1405	CGCG 436-030	01h20m02.72s	+14d21m42.9s	9362	134.0	11.69
F01325-3623	ESO 353-G020	01h34m51.28s	-36d08m14.0s	4797	68.8	11.06
F01341-3735	RR 032	01h36m23.79s	-37d19m51.7s	5191	74.6	11.16:
F01364-1042		01h38m52.92s	-10d27m11.4s	14464	210.0	11.85:
F01417+1651	III Zw 035	01h44m30.45s	+17d06m05.0s	8375	119.0	11.64:
F01484+2220	NGC 0695	01h51m14.24s	+22d34m56.5s	9735	139.0	11.68
F01519+3640	UGC 01385	01h54m53.79s	+36d55m04.6s	5621	79.8	11.05:
F02071-1023	NGC 0838	02h09m38.58s	-10d08m46.3s	3851	53.8	11.05:
F02070+3857	NGC 0828	02h10m09.57s	+39d11m25.3s	5374	76.3	11.36
F02114+0456	IC 0214	02h14m05.59s	+05d10m23.7s	9061	129.0	11.43
F02152+1418	NGC 0877	02h17m59.64s	+14d32m38.6s	3913	54.6	11.10
F02203+3158	MCG +05-06-036	02h23m21.99s	+32d11m49.5s	10106	145.0	11.64
F02208+4744	UGC 01845	02h24m07.98s	+47d58m11.0s	4679	67.0	11.12
F02281-0309	NGC 0958	02h30m42.83s	-02d56m20.4s	5738	80.6	11.20
F02345+2053	NGC 0992	02h37m25.49s	+21d06m03.0s	4141	58.0	11.07
F02401-0013	NGC 1068	02h42m40.71s	-00d00m47.8s	1137	15.9	11.40
F02435+1253	UGC 02238	02h46m17.49s	+13d05m44.4s	6560	92.4	11.33:
F02437+2122		02h46m39.15s	+21d35m10.3s	6987	98.8	11.16:
F02512+1446	UGC 02369	02h54m01.78s	+14d58m24.9s	9558	136.0	11.67
F03117+4151	UGC 02608	03h15m01.42s	+42d02m09.4s	6998	100.0	11.41
F03164+4119	NGC 1275	03h19m48.16s	+41d30m42.1s	5264	75.0	11.26
F03217+4022		03h25m05.38s	+40d33m29.0s	7007	100.0	11.33
F03316-3618	NGC 1365	03h33m36.37s	-36d08m25.4s	1636	17.9	11.00
F03359+1523		03h38m46.70s	+15d32m55.0s	10613	152.0	11.55:
F03514+1546	CGCG 465-012	03h54m16.08s	+15d55m43.4s	6662	94.3	11.20:
03582+6012		04h02m32.48s	+60d20m40.1s	8997	131.0	11.43:
F04097+0525	UGC 02982	04h12m22.45s	+05d32m50.6s	5305	74.9	11.20
F04118-3207	ESO 420-G013	04h13m49.69s	-32d00m25.1s	3570	51.0	11.07
F04191-1855	ESO 550-IG 025	04h21m20.02s	-18d48m47.6s	9621	138.5	11.51
F04210-4042	NGC 1572	04h22m42.81s	-40d36m03.3s	6111	88.6	11.30
04271+3849		04h30m33.09s	+38d55m47.7s	5640	80.8	11.11:
F04315-0840	NGC 1614	04h33m59.85s	-08d34m44.0s	4778	67.8	11.65
F04326+1904	UGC 03094	04h35m33.83s	+19d10m18.2s	7408	106.0	11.41
F04454-4838	ESO 203-IG001	04h46m49.50s	-48d33m32.9s	15862	235.0	11.86:
F04502-3304	MCG -05-12-006	04h52m04.96s	-32d59m25.6s	5622	81.3	11.17
F05053-0805	NGC 1797	05h07m44.88s	-08d01m08.7s	4441	63.4	11.04
F05054+1718	CGCG 468-002	05h08m20.5s	+17d21m58s	5454	77.9	11.22
05083+2441		05h11m25.88s	+24d45m18.3s	6915	99.2	11.26:
F05081+7936	VII Zw 031	05h16m46.44s	+79d40m12.6s	16090	240.0	11.99
05129+5128		05h16m56.10s	+51d31m56.5s	8224	120.0	11.42
F05189-2524		05h21m01.47s	-25d21m45.4s	12760	187.0	12.16
F05187-1017		05h21m06.54s	-10d14m46.7s	8474	122.0	11.30:
05223+1908		05h25m16.50s	+19d10m46.0s	8867	128.0	11.65:
05368+4940	MCG +08-11-002	05h40m43.71s	+49d41m41.5s	5743	83.7	11.46
F05365+6921	NGC 1961	05h42m04.65s	+69d22m42.4s	3934	59.0	11.06
F05414+5840	UGC 03351	05h45m47.88s	+58d42m03.9s	4455	65.8	11.28
05442+1732		05h47m11.18s	+17d33m46.7s	5582	80.5	11.30
F06076-2139		06h09m45.81s	-21d40m23.7s	11226	165.0	11.65
F06052+8027	UGC 03410	06h14m29.63s	+80d26m59.6s	3921	59.7	11.10:
F06107+7822	NGC 2146	06h18m37.71s	+78d21m25.3s	893	17.5	11.12
F06259-4708	ESO 255-IG007	06h27m22.45s	-47d10m48.7s	11629	173.0	11.90
F06295-1735	ESO 557-G002	06h31m47.22s	-17d37m17.3s	6385	93.6	11.25
F06538+4628	UGC 3608	06h57m34.45s	+46d24m10.8s	6401	94.3	11.34
F06592-6313		06h59m40.25s	-63d17m52.9s	6882	104.0	11.24
F07027-6011	AM 0702-601	07h03m26.37s	-60d16m03.7s	9390	141.0	11.64
07063+2043	NGC 2342	07h09m18.08s	+20d38m09.5s	5276	78.0	11.31:
F07160-6215	NGC 2369	07h16m37.73s	-62d20m37.4s	3240	47.6	11.16
07251-0248		07h27m37.55s	-02d54m54.1s	26249	400.0	12.39:
F07256+3355	NGC 2388	07h28m53.44s	+33d49m08.7s	4134	62.1	11.28:
F07329+1149	MCG +02-20-003	07h35m43.37s	+11d42m33.5s	4873	72.8	11.13:
08355-4944		08h37m01.82s	-49d54m30.2s	7764	118.0	11.62
F08339+6517		08h38m23.18s	+65d07m15.2s	5730	86.3	11.11
F08354+2555	NGC 2623	08h38m24.08s	+25d45m16.6s	5549	84.1	11.60
08424-3130	ESO 432-IG006	08h44m28.07s	-31d41m40.6s	4846	74.4	11.08
F08520-6850	ESO 060-IG 016	08h52m31.29s	-69d01m57.0s	13885	210.0	11.82:

TABLE 1
The GOALS Sample

F08572+3915		09h00m25.39s	+39d03m54.4s	17493	264.0	12.16
09022-3615		09h04m12.70s	-36d27m01.1s	17880	271.0	12.31
F09111-1007		09h13m37.61s	-10d19m24.8s	16231	246.0	12.06
F09126+4432	UGC 04881	09h15m55.11s	+44d19m54.1s	11851	178.0	11.74
F09320+6134	UGC 05101	09h35m51.65s	+61d21m11.3s	11802	177.0	12.01:
F09333+4841	MCG +08-18-013	09h36m37.19s	+48d28m27.7s	7777	117.0	11.34
F09437+0317	Arp 303	09h46m20.71s	+03d03m30.5s	5996	92.9	11.23:
F10015-0614	NGC 3110	10h04m02.11s	-06d28m29.2s	5054	79.5	11.37:
F10038-3338	ESO 374-IG 032[a]	10h06m04.8s	-33d53m15.0s	10223	156.0	11.78
F10173+0828		10h20m00.21s	+08d13m33.8s	14716	224.0	11.86
F10196+2149	NGC 3221	10h22m19.98s	+21d34m10.5s	4110	65.7	11.09
F10257-4339	NGC 3256	10h27m51.27s	-43d54m13.8s	2804	38.9	11.64
F10409-4556	ESO 264-G036	10h43m07.67s	-46d12m44.6s	6299	100.0	11.32
F10567-4310	ESO 264-G057	10h59m01.79s	-43d26m25.7s	5156	83.3	11.14:
F10565+2448		10h59m18.14s	+24d32m34.3s	12921	197.0	12.08
F11011+4107	MCG +07-23-019	11h03m53.20s	+40d50m57.0s	10350	158.0	11.62
F11186-0242	CGCG 011-076	11h21m12.26s	-02d59m03.5s	7464	117.0	11.43
F11231+1456		11h25m47.30s	+14d40m21.1s	10192	157.0	11.64
F11255-4120	ESO 319-G022	11h27m54.08s	-41d36m52.4s	4902	80.0	11.12
F11257+5850	NGC 3690	11h28m32.25s	+58d33m44.0s	3093	50.7	11.93
F11506-3851	ESO 320-G030	11h53m11.72s	-39d07m48.9s	3232	41.2	11.17
F12043-3140	ESO 440-IG058	12h06m51.82s	-31d56m53.1s	6956	112.0	11.43
F12112+0305		12h13m46.00s	+02d48m38.0s	21980	340.0	12.36:
F12116+5448	NGC 4194	12h14m09.47s	+54d31m36.6s	2501	43.0	11.10
F12115-4656	ESO 267-G030	12h14m12.84s	-47d13m43.2s	5543	97.1	11.25:
12116-5615		12h14m22.10s	-56d32m33.2s	8125	128.0	11.65
F12224-0624		12h25m03.91s	-06d40m52.6s	7902	125.0	11.36:
F12243-0036	NGC 4418	12h26m54.62s	-00d52m39.2s	2179	36.5	11.19
F12540+5708	UGC 08058	12h56m14.24s	+56d52m25.2s	12642	192.0	12.57
F12590+2934	NGC 4922	13h01m24.89s	+29d18m40.0s	7071	111.0	11.38
F12592+0436	CGCG 043-099	13h01m50.80s	+04d20m00.0s	11237	175.0	11.68
F12596-1529	MCG -02-33-098	13h02m19.70s	-15d46m03.0s	4773	78.7	11.17
F13001-2339	ESO 507-G070	13h02m52.35s	-23d55m17.7s	6506	106.0	11.56
13052-5711		13h08m18.73s	-57d27m30.2s	6364	106.0	11.40:
F13126+2453	IC 0860	13h15m03.53s	+24d37m07.9s	3347	56.8	11.14:
13120-5453		13h15m06.35s	-55d09m22.7s	9222	144.0	12.32
F13136+6223	VV 250a	13h15m35.06s	+62d07m28.6s	9313	142.0	11.81
F13182+3424	UGC 08387	13h20m35.34s	+34d08m22.2s	6985	110.0	11.73
F13188+0036	NGC 5104	13h21m23.08s	+00d20m32.7s	5578	90.8	11.27
F13197-1627	MCG -03-34-064	13h22m24.46s	-16d43m42.9s	4959	82.2	11.28
F13229-2934	NGC 5135	13h25m44.06s	-29d50m01.2s	4105	60.9	11.30
13242-5713	ESO 173-G015	13h27m23.78s	-57d29m22.2s	2918	34.0	11.38:
F13301-2356	IC 4280	13h32m53.40s	-24d12m25.7s	4889	82.4	11.15
F13362+4831	NGC 5256	13h38m17.52s	+48d16m36.7s	8341	129.0	11.56
F13373+0105	Arp 240	13h39m55.00s	+00d50m07.0s	6778	108.5	11.62
F13428+5608	UGC 08696	13h44m42.11s	+55d53m12.6s	11326	173.0	12.21
F13470+3530	UGC 08739	13h49m13.93s	+35d15m26.8s	5032	81.4	11.15:
F13478-4848	ESO 221-IG010	13h50m56.94s	-49d03m19.5s	3099	62.9	11.22
F13497+0220	NGC 5331	13h52m16.29s	+02d06m17.0s	9906	155.0	11.66
F13564+3741	Arp 84	13h58m35.81s	+37d26m20.3s	3482	58.7	11.08
F14179+4927	CGCG 247-020	14h19m43.25s	+49d14m11.7s	7716	120.0	11.39
F14280+3126	NGC 5653	14h30m10.42s	+31d12m55.8s	3562	60.2	11.13
F14348-1447		14h37m38.37s	-15d00m22.8s	24802	387.0	12.39:
F14378-3651		14h40m59.01s	-37d04m32.0s	20277	315.0	12.23:
F14423-2039	NGC 5734	14h45m09.05s	-20d52m13.7s	4121	67.1	11.15:
F14547+2449	VV 340a	14h57m00.68s	+24d37m02.7s	10094	157.0	11.74
F14544-4255	IC 4518	14h57m42.82s	-43d07m54.3s	4763	80.0	11.23
F15107+0724	CGCG 049-057	15h13m13.09s	+07d13m31.8s	3897	65.4	11.35:
F15163+4255	VV 705	15h18m06.28s	+42d44m41.2s	11944	183.0	11.92
15206-6256	ESO 099-G004	15h24m58.19s	-63d07m34.2s	8779	137.0	11.74
F15250+3608		15h26m59.40s	+35d58m37.5s	16535	254.0	12.08
F15276+1309	NGC 5936	15h30m00.84s	+12d59m21.5s	4004	67.1	11.14
F15327+2340	UGC 09913	15h34m57.12s	+23d30m11.5s	5434	87.9	12.28
F15437+0234	NGC 5990	15h46m16.37s	+02d24m55.7s	3839	64.4	11.13
F16030+2040	NGC 6052	16h05m13.05s	+20d32m32.6s	4739	77.6	11.09
F16104+5235	NGC 6090	16h11m40.70s	+52d27m24.0s	8947	137.0	11.58
F16164-0746		16h19m11.79s	-07d54m02.8s	8140	128.0	11.62:
F16284+0411	CGCG 052-037	16h30m56.54s	+04d04m58.4s	7342	116.0	11.45
16304-6030	NGC 6156	16h34m52.55s	-60d37m07.7s	3263	48.0	11.14
F16330-6820	ESO 069-IG006	16h38m12.65s	-68d26m42.6s	13922	212.0	11.98
F16399-0937		16h42m40.21s	-09d43m14.4s	8098	128.0	11.63:
F16443-2915	ESO 453-G005	16h47m31.06s	-29d21m21.6s	6260	100.0	11.37:
F16504+0228	NGC 6240	16h52m58.89s	+02d24m03.4s	7339	116.0	11.93
F16516-0948		16h54m24.03s	-09d53m20.9s	6755	107.0	11.31:
F16577+5900	NGC 6286	16h58m31.38s	+58d56m10.5s	5501	85.7	11.37
F17132+5313		17h14m20.00s	+53d10m30.0s	15270	232.0	11.96
F17138-1017		17h16m35.79s	-10d20m39.4s	5197	84.0	11.49
F17207-0014		17h23m21.95s	-00d17m00.9s	12834	198.0	12.46:
F17222-5953	ESO 138-G027	17h26m43.34s	-59d55m55.3s	6230	98.3	11.41

TABLE 1
The GOALS Sample

F17530+3447	UGC 11041	17h54m51.82s	+34d46m34.4s	4881	77.5	11.11
F17548+2401	CGCG 141-034	17h56m56.63s	+24d01m01.6s	5944	93.4	11.20
17578-0400		18h00m31.90s	-04d00m53.3s	4210	68.5	11.48:
18090+0130		18h11m35.91s	+01d31m41.3s	8662	134.0	11.65:
F18131+6820	NGC 6621	18h12m55.31s	+68d21m48.4s	6191	94.3	11.29
F18093-5744	IC 4687	18h13m39.63s	-57d43m31.3s	5200	81.9	11.62:
F18145+2205	CGCG 142-034	18h16m40.66s	+22d06m46.1s	5599	88.1	11.18
F18293-3413		18h32m41.13s	-34d11m27.5s	5449	86.0	11.88
F18329+5950	NGC 6670	18h33m35.91s	+59d53m20.2s	8574	129.5	11.65
F18341-5732	IC 4734	18h38m25.70s	-57d29m25.6s	4680	73.4	11.35
F18425+6036	NGC 6701	18h43m12.46s	+60d39m12.0s	3965	62.4	11.12
F19120+7320	VV 414	19h10m59.20s	+73d25m06.3s	7528	113.0	11.49
F19115-2124	ESO 593-IG008	19h14m30.90s	-21d19m07.0s	14608	222.0	11.93
F19297-0406		19h32m21.25s	-03d59m56.3s	25701	395.0	12.45:
19542+1110		19h56m35.44s	+11d19m02.6s	19473	295.0	12.12:
F19542-3804	ESO 339-G011	19h57m37.54s	-37d56m08.4s	5756	88.6	11.20
F20221-2458	NGC 6907	20h25m06.65s	-24d48m33.5s	3190	50.1	11.11
20264+2533	MCG +04-48-002	20h28m35.06s	+25d44m00.0s	4167	64.2	11.11
F20304-0211	NGC 6926	20h33m06.11s	-02d01m39.0s	5880	89.1	11.32
20351+2521		20h37m17.72s	+25d31m37.7s	10102	151.0	11.61
F20550+1655	CGCG 448-020	20h57m23.90s	+17d07m39.0s	10822	161.0	11.94
F20551-4250	ESO 286-IG019	20h58m26.79s	-42d39m00.3s	12890	193.0	12.06
F21008-4347	ESO 286-G035	21h04m11.18s	-43d35m33.0s	5205	79.1	11.20:
21101+5810		21h11m30.40s	+58d23m03.2s	11705	174.0	11.81:
F21330-3846	ESO 343-IG013	21h36m10.83s	-38d32m37.9s	5714	85.8	11.14
F21453-3511	NGC 7130	21h48m19.50s	-34d57m04.7s	4842	72.7	11.42
F22118-2742	ESO 467-G027	22h14m39.92s	-27d27m50.3s	5217	77.3	11.08
F22132-3705	IC 5179	22h16m09.10s	-36d50m37.4s	3422	51.4	11.24
F22287-1917	ESO 602-G025	22h31m25.48s	-19d02m04.1s	7507	110.0	11.34
F22389+3359	UGC 12150	22h41m12.26s	+34d14m57.0s	6413	93.5	11.35
F22467-4906	ESO 239-IG002	22h49m39.87s	-48d50m58.1s	12901	191.0	11.84
F22491-1808		22h51m49.26s	-17d52m23.5s	23312	351.0	12.20:
F23007+0836	NGC 7469	23h03m15.62s	+08d52m26.4s	4892	70.8	11.65
F23024+1916	CGCG 453-062	23h04m56.53s	+19d33m08.0s	7524	109.0	11.38:
F23128-5919	ESO 148-IG002	23h15m46.78s	-59d03m15.6s	13371	199.0	12.06
F23135+2517	IC 5298	23h16m00.70s	+25d33m24.1s	8221	119.0	11.60
F23133-4251	NGC 7552	23h16m10.77s	-42d35m05.4s	1608	23.5	11.11
F23157+0618	NGC 7591	23h18m16.28s	+06d35m08.9s	4956	71.4	11.12
F23157-0441	NGC 7592	23h18m22.20s	-04d24m57.6s	7328	106.0	11.40
F23180-6929	ESO 077-IG014	23h21m04.53s	-69d12m54.2s	12460	186.0	11.76
F23254+0830	NGC 7674	23h27m56.72s	+08d46m44.5s	8671	125.0	11.56
23262+0314	NGC 7679	23h28m46.66s	+03d30m41.1s	5138	73.8	11.11
F23365+3604		23h39m01.27s	+36d21m08.7s	19331	287.0	12.20:
F23394-0353	MCG -01-60-022	23h42m00.85s	-03d36m54.6s	6966	100.0	11.27
23436+5257		23h46m05.58s	+53d14m00.6s	10233	149.0	11.57:
F23444+2911	Arp 86	23h47m01.70s	+29d28m16.3s	5120	73.6	11.07
F23488+1949	NGC 7771	23h51m24.88s	+20d06m42.6s	4277	61.2	11.40
F23488+2018	MRK 0331	23h51m26.80s	+20d35m09.9s	5541	79.3	11.50

Note. — Column (1): Original IRAS source, where an "F" prefix indicates the Faint Source Catalog and no prefix indicates the Point Source Catalog. Column (2): Optical cross-identification, where available from NED. For many cases where the IRAS source corresponds to a pair of optically identified galaxies, we adopt the system name instead of pair components. For example, IRAS F00163-1039 is identified in GOALS as Arp 256 rather than "MCG -02-01-051/2" as in Sanders et al. 2003. Column (3): The best available source right ascension (J2000) in NED as of October 2008. Column (4): The best available source declination (J2000) in NED as of October 2008. Column (5): The best available heliocentric redshift, expressed as a velocity, in NED as of October 2008. Column (6): The luminosity distance in megaparsecs derived by correcting the heliocentric velocity for the 3-attractor flow model of Mould et al. (2000) and adopting cosmological parameters $H_0 = 70$ km s^{-1} Mpc^{-1}, $\Omega_{Vacuum} = 0.72$, and $\Omega_{Matter} = 0.28$ based on the five-year WMAP results (Hinshaw et al. 2009), as provided by NED. Column (7): The total infrared luminosity in $\log_{10}$ Solar units computed using the flux densities reported in the RBGS and the lumiosity distances in column (6) using the formulae $L_{ir}/L_\odot = 4\pi(D_L[m])^2 (F_{ir} [W\ m^{-2}])/3.826 \times 10^{26}[Wm^{-2}]$, where $F_{ir} = 1.8 \times 10^{-14}\{13.48f_{12\mu m} + 5.16f_{25\mu m} + 2.58f_{60\mu m} + f_{100\mu m}[Wm^{-2}]\}$ (Sanders & Mirabel 1996); colons indicate uncertain IRAS measurements (Sanders, et al. 2003).
[a] When the IRAS Revised Bright Galaxy Sample (RBGS, Sanders et al. 2003) was compiled, IRAS F10038-3338 was mistakenly cross-identified with the optical source IC 2545. The proper optical counterpart is ESO 374-IG 032. (See the Essential Notes in NED.)

TABLE 2
GOALS Data Sets

Type (1)	Wavelength/Filter (2)	Observatory (3)	Number (4)
X-Ray Imaging & Spectroscopy	$0.4 - 7$ keV	Chandra - ACIS	44
Ultraviolet imaging	1528Å(FUV), 2271Å(NUV)	GALEX	124
Ultraviolet imaging	1400Å(F140LP)	Hubble - ACS/SBC	30
Ultraviolet imaging	2180Å(F218W)	Hubble - WFPC2	30
Visual imaging	4350Å(F435W), 8140Å(F814W)	Hubble - ACS	88
Near-Infrared imaging	$1.6\mu m$ (F160W)	Hubble - NICMOS	88
Mid-Infrared imaging	3.6, 4.5, 5.4, $8\mu m$	Spitzer - IRAC	202
Mid-Infrared nuclear spectroscopy	$5 - 40\mu m$ low-res, $10 - 40\mu m$ high-res	Spitzer - IRS	202
Mid-Infrared spectral mapping	$5-40\mu m$ low-res	Spitzer - IRS	42
Far-Infrared imaging	24,70,160μm	Spitzer - MIPS	202

Note. — Summary of the primary (Spitzer, Chandra, Hubble and GALEX) GOALS data sets. The type of data, the wavelengths covered, the observatory, and the number of LIRGs (systems) observed (including archival data) are given in cols. 1-4, respectively. Ancillary data is discussed in the text.